Chaos and ergodicity of two hard disks within a circular billiard

Shin-ichi Sawada* and Tooru Taniguchi
Department of Physics, Kwansei Gakuin University, Sanda 669-1337, Japan
(Received 17 May 2013; published 7 August 2013)

We investigate dynamical properties of the system of two interacting hard disks within a circular billiard numerically in the case of zero total angular momentum. Varying the radius of two identical disks, we examine chaotic irregularity and ergodicity of the system. Single-particle configuration and velocity distributions are obtained from dynamical trajectory calculations and compared with those in the microcanonical ensemble. We also analyze properties of trajectories by calculating the finite-time maximum Lyapunov exponent and clarify the existence of sticky motions around Kolmogorov-Arnold-Moser (KAM) tori even for small radii of disks. It is shown that the present system is almost ergodic in spite of the existence of tori for small radii of disks since the ratio of tori to the whole phase space is extremely small. On the other hand, a number of tori increase abruptly as the radius of disks increases beyond some value and tori prevent trajectories to run over the phase space uniformly, which makes the ergodicity of the system broken down.

DOI: 10.1103/PhysRevE.88.022907 PACS number(s): 05.45.−a, 05.10.−a

I. INTRODUCTION

There have been numerous studies on ergodicity and chaos in conservative Hamiltonian systems through both analytical and numerical approaches. Those studies are very important to understand the mechanism of irregular and unpredictable behaviors of Hamiltonian systems and their ergodicity, which provides the validity of the statistical mechanics [1–4]. Numerical studies of ergodicity are over various systems, e.g, Henon-Heiles system, a few-body hard core system, Fermi-Pasta-Ulam model, and so on [5,6]. On the other hand, rigorous mathematical investigations are very limited. There are a small number of systems whose ergodicity has been proved, e.g., the stadium billiard, the Sinai billiard, the Lorentz gas, etc. [3–5,7,8]. Typical Hamiltonian systems exhibit mixed dynamics, whose phase spaces contain islands of stability, Kolmogorov-Arnold-Moser (KAM) tori, in a chaotic sea. However, rigorous mathematical methods have not been well developed to reveal dynamical structures of such systems. Therefore, numerical studies on mixed systems are still very important.

Billiard systems are primary examples used to study classical and quantum chaos of the Hamiltonian systems [7–9]. However, in spite of an accumulation of studies on billiard systems, most of them are limited to the systems of a single point particle or a single disk confined in billiards. There exist much fewer works on billiards which contain mutually interacting few-body particles. On the other hand, from both the theoretical and experimental points of view, systems of a few particles are getting increasing attention because of nanoscience and possible applications in nanotechnology. Especially on the theoretical side, a remarkable point is that a few-particle billiard exhibits possibly both regular and chaotic features depending on the geometry of the billiard boundary and the confined particles [10–12]. Statistical mechanical properties of systems with a few hard disks or spheres have been studied by several authors [13]. This paper is rather concerned with chaotic dynamics and ergodic properties of such systems.

The system consisting of two identical hard disks in a rectangular billiard have been shown to be ergodic for smaller radii of disks numerically by Zheng *et al.* [14]. Later, the ergodicity of this system has been proved analytically and rigorously by Simányi [15]. Simányi's result has been extended to several billiard systems having polygon boundaries by other authors [16]. On the other hand, as for the system consisting of two identical hard disks in a circular billiard, its ergodicity (or nonergodicity) has not been clarified yet. This system is considered to have mixed dynamics and its analytical investigation is quite difficult. Lansel *et al.* examined its dynamics numerically and obtained asymmetric distributions of incident angles at collisions between hard disks and a boundary, from which they suggested nonergodicity of this system [11]. Uranagase compared the pressure of this system evaluated by trajectory calculations with that derived from the microcanonical ensemble [17]. He found a large statistical fluctuation of the pressure evaluated by trajectory calculations for a relatively large radius of disks and suggested nonergodicity of this system. However, these two works have not revealed its nonergodicity clearly. Nakazono *et al.* calculated the maximum Lyapunov exponent as a function of the radius of disks in this system and found it to depend on initial conditions [18]. It has a maximum value for the radius of disks $\sigma \simeq 0.25$ (the radius of a billiard is unity), above which its standard deviation increases as a radius increases. From this fact they claimed that the ergodicity is not guaranteed for $\sigma \gtrsim 0.25$. They just mentioned without showing any numerical evidences that there exist tori in the full range of σ and, however, their ratio to the whole phase space is extremely small. The main subject of their work is a quantum dynamics of this system. They found that the energy-level-space distribution is consistent with the Wigner distribution in the full range of σ, which suggests a strong chaotic property of this system.

In this paper, we investigate classical dynamical properties of the system of two identical hard disks within a circular billiard numerically. We confine our studies to the case of zero total angular momentum. Varying the radius of each disk, we examine chaotic irregularity and ergodicity of the system. In order to analyze dynamical properties of the system, we

*s-sawada@kwansei.ac.jp

 ©2013 American Physical Society

compare single-particle configuration and velocity distributions obtained from dynamical trajectory calculations with those derived from the microcanonical ensemble for various radii of the hard disks. We also calculate time evolution of the finite-time maximum Lyapunov exponents along trajectories. From those results we show that for even small radii of disks this system exhibits mixed dynamics including sticky motions around tori. Moreover, we examine whether the trajectories run over the phase space uniformly. Consequently, we show that this system is not fully chaotic but still almost ergodic for smaller radii of disks, while it has a strongly nonergodic property for larger radii of disks.

The organization of the paper is as follows: In Sec. II, we introduce the model system and describe some methods for analyzing its dynamics. The results for numerical calculations are given in Sec. III. Section IV is concerned with summary and discussion.

II. MODEL AND METHOD

We consider a system of two identical hard disks within a circular billiard. The disks make a ballistic motion except bouncing with each other and with the billiard boundary. We choose a radius of the billiard to be unity without loss of generality. Varying the radius of each disk σ, we examine the chaotic irregularity and ergodicity of the system. The total energy E and total angular momentum of the system L are given by

$$E = \tfrac{1}{2}m\left(v_{x,1}^2 + v_{y,1}^2 + v_{x,2}^2 + v_{y,2}^2\right) \tag{1}$$

and

$$L = m(x_1 v_{y,1} - y_1 v_{x,1} + x_2 v_{y,2} - y_2 v_{x,2}), \tag{2}$$

respectively, where m, (x_i, y_i) and $(v_{x,i}, v_{y,i})(i = 1,2)$ are the mass, coordinates, and velocities of the hard disks, respectively. The total angular momentum is conserved due to circular symmetry of the system. In this paper, we are concerned with only the case of zero total angular momentum and scale velocities by $\sqrt{E/m}$. Thus, Eqs. (1) and (2) are reduced to

$$v_{x,1}^2 + v_{y,1}^2 + v_{x,2}^2 + v_{y,2}^2 = 2 \tag{3}$$

and

$$x_1 v_{y,1} - y_1 v_{x,1} + x_2 v_{y,2} - y_2 v_{x,2} = 0, \tag{4}$$

respectively. If the system is ergodic, both configuration and velocity distributions obtained from a single trajectory with almost any initial condition are consistent with those derived from the microcanonical ensemble. The microcanonical ensemble distribution is written as

$$\begin{aligned}&\rho(x_1, y_1, x_2, y_2, v_{x,1}, v_{y,1}, v_{x,2}, v_{y,2})\\ &\quad = C_N \delta\left(2 - v_{x,1}^2 - v_{y,1}^2 - v_{x,2}^2 - v_{y,2}^2\right)\\ &\qquad \times \delta(x_1 v_{y,1} - y_1 v_{x,1} + x_2 v_{y,2} - y_2 v_{x,2}),\end{aligned} \tag{5}$$

where C_N is a normalization constant. The single-particle configuration and velocity distribution functions are given by

$$\begin{aligned}F(x,y) = \int \cdots \int \rho(x_1, y_1, x, y, v_{x,1}, v_{y,1}, v_{x,2}, v_{y,2})\\ \times dv_{x,1} dv_{y,1} dv_{x,2} dv_{y,2} dx_1 dy_1\end{aligned} \tag{6}$$

and

$$\begin{aligned}G(v_x, v_y) = \int \cdots \int \rho(x_1, y_1, x_2, y_2, v_{x,1}, v_{y,1}, v_x, v_y)\\ \times dv_{x,1} dv_{y,1} dx_1 dy_1 dx_2 dy_2,\end{aligned} \tag{7}$$

respectively. We compare single-particle distribution functions obtained from dynamical trajectory calculations with them.

In order to characterize the chaotic property of the system, we calculate the finite-time maximum Lyapunov exponent (FTMLE) defined by

$$\lambda(t_0, t) = \frac{1}{t - t_0} \lim_{d_0 \to 0} \ln \frac{d(t)}{d_0}, \tag{8}$$

where d_0 and $d(t)$ are the separations between two adjacent trajectories at time t_0 and t, respectively. The ordinary (i.e., infinite-time) Lyapunov exponent is given in the limit of $t \to \infty$ in Eq. (8). However, the convergence is quite slow in the generic system and, moreover, values of FTMLE depend on the initial condition. This is the case in the present system as shown in the next section. It implies that chaotic and regular motions coexist even along a single trajectory in the present system. We display this point clearly by examining FTMLE and relating it with the ergodicity of the system.

Now, we turn back to the single-particle distribution functions and derive their detailed expressions. First, we calculate the two-particle configuration distribution function

$$\begin{aligned}&f(x_1, y_1, x_2, y_2)\\ &\quad \propto \int_{-\infty}^{\infty} \cdots \int_{-\infty}^{\infty} \delta\left(2 - v_{x,1}^2 - v_{y,1}^2 - v_{x,2}^2 - v_{y,2}^2\right) \delta(x_1 v_{y,1}\\ &\qquad - y_1 v_{x,1} + x_2 v_{y,2} - y_2 v_{x,2}) dv_{x,1} dv_{y,1} dv_{x,2} dv_{y,2}.\end{aligned} \tag{9}$$

Changing the variables $v_{x,i}$ and $v_{y,i}$ to U_i and V_i defined by $U_i = (y_i v_{x,i} - x_i v_{y,i})/r_i$ and $V_i = (x_i v_{x,i} + y_i v_{y,i})/r_i$ with $r_i = \sqrt{x_i^2 + y_i^2}$ $(i = 1,2)$, we have

$$\begin{aligned}f(x_1, y_1, x_2, y_2) \propto \int_{-\infty}^{\infty} \cdots \int_{-\infty}^{\infty} \delta(2 - U_1^2 - V_1^2 - U_2^2 - V_2^2)\\ \times \delta(r_1 U_1 + r_2 U_2) dU_1 dV_1 dU_2 dV_2.\end{aligned} \tag{10}$$

We further change U_1 and U_2 to ξ and η defined by $\xi = (r_2 U_1 - r_1 U_2)/R$ and $\eta = (r_1 U_1 + r_2 U_2)/R$ with $R = \sqrt{r_1^2 + r_2^2}$. Then, we obtain

$$\begin{aligned}&f(x_1, y_1, x_2, y_2)\\ &\quad \propto \int_{-\infty}^{\infty} \cdots \int_{-\infty}^{\infty} \delta\left(2 - \xi^2 - \eta^2 - V_1^2 - V_2^2\right)\\ &\qquad \times \delta(R\eta) d\xi\, d\eta\, dV_1 dV_2\\ &\quad \propto \frac{1}{R} \int_{-\infty}^{\infty} \cdots \int_{-\infty}^{\infty} \delta\left(2 - \xi^2 - V_1^2 - V_2^2\right) d\xi\, dV_1 dV_2\\ &\quad \propto \frac{1}{R} \iiint \delta(Q^2 - \xi^2) d\xi\, dV_1 dV_2\\ &\quad \propto \frac{2}{R} \iint \frac{1}{Q} dV_1 dV_2,\end{aligned} \tag{11}$$

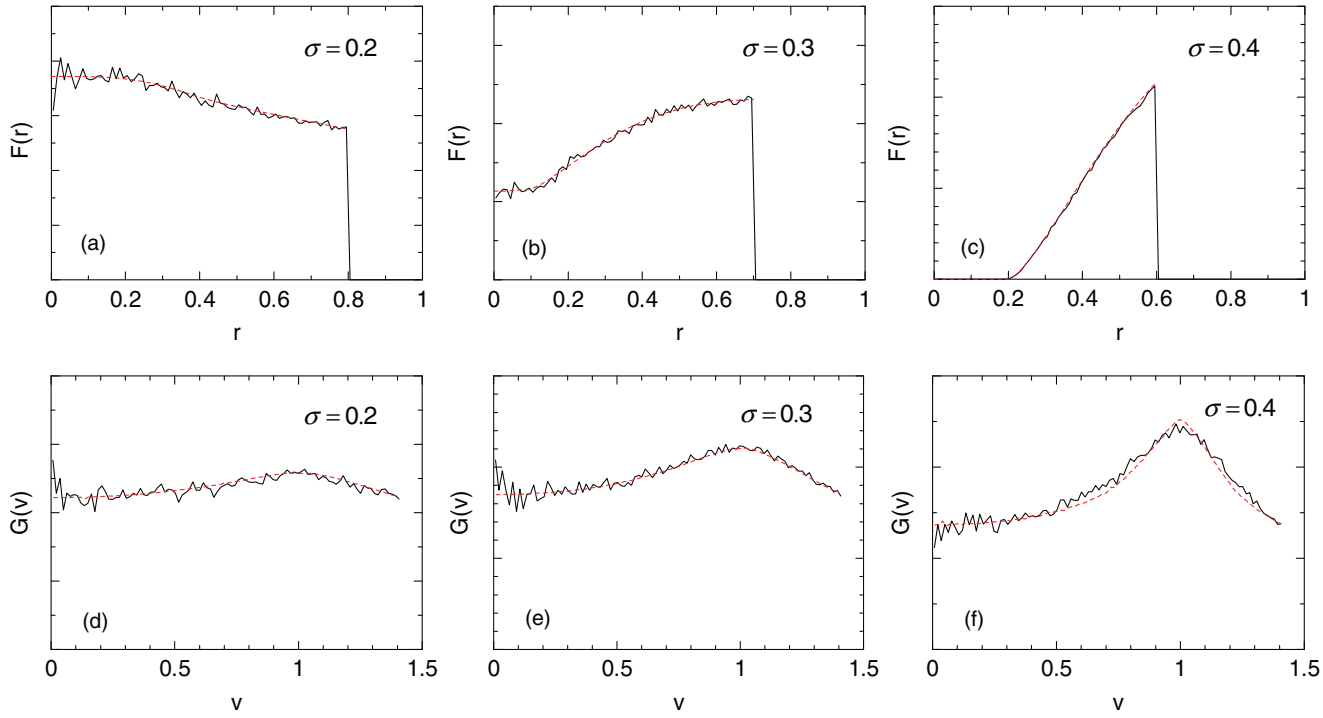

FIG. 1. (Color online) The single-particle configuration distributions (upper panels) and velocity distributions (lower panels). The solid and broken curves are from sampling and the microcanonical ensemble, respectively.

where $Q = \sqrt{2 - V_1^2 - V_2^2}$. Consequently, Eq. (9) is reduced to

$$f(x_1, y_1, x_2, y_2) \propto \frac{1}{\sqrt{r_1^2 + r_2^2}}. \tag{12}$$

The single-particle configuration distribution function (6) is given by

$$F(x, y) \propto \iint_D \frac{1}{\sqrt{r^2 + r_2^2}} dx_2 dy_2, \tag{13}$$

where $r = \sqrt{x^2 + y^2}$ and $r_2 = \sqrt{x_2^2 + y_2^2}$. The domain of integration D is the accessible area of the second disk centered at $(x_2,\ y_2)$ when the first disk is centered at $(x,\ y)$ within the circular billiard. Detailed numerical techniques of the integration are described in Appendix A. Hereafter, we use the expression $F(r)$ instead of $F(x, y)$ since it has circular symmetry.

Next, we calculate the single-particle velocity distribution function

$$\begin{aligned} G(v_x, v_y) \propto \int \dots \int & \delta\left(2 - v_{x,1}^2 - v_{y,1}^2 - v_x^2 - v_y^2\right) \\ & \times \delta(x_1 v_{y,1} - y_1 v_{x,1} + x_2 v_y - y_2 v_x) \\ & \times dv_{x,1} dv_{y,1} dx_1 dy_1 dx_2 dy_2. \end{aligned} \tag{14}$$

Changing the variables $v_{x,1}$ and $v_{y,1}$ to U and V defined by $U = (y_1 v_{x,1} - x_1 v_{y,1})/r_1$ and $V = (x_1 v_{x,1} + y_1 v_{y,1})/r_1$ with

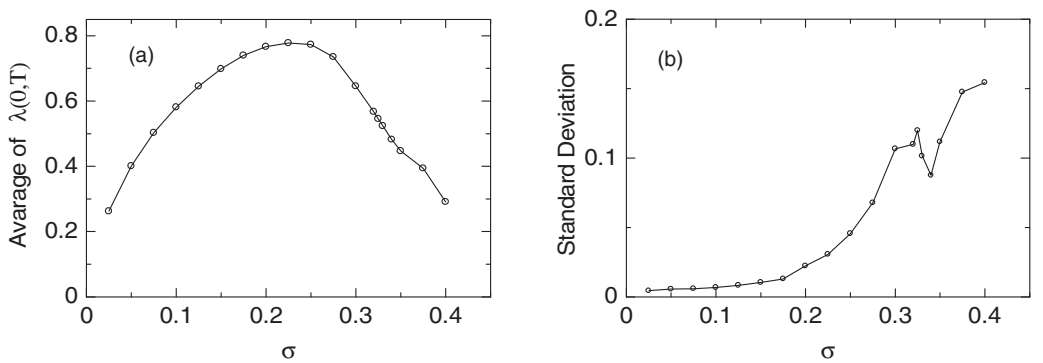

FIG. 2. The averaged values (a) and standard deviation (b) of FTMLE $\lambda(0, T)$ for various σ.

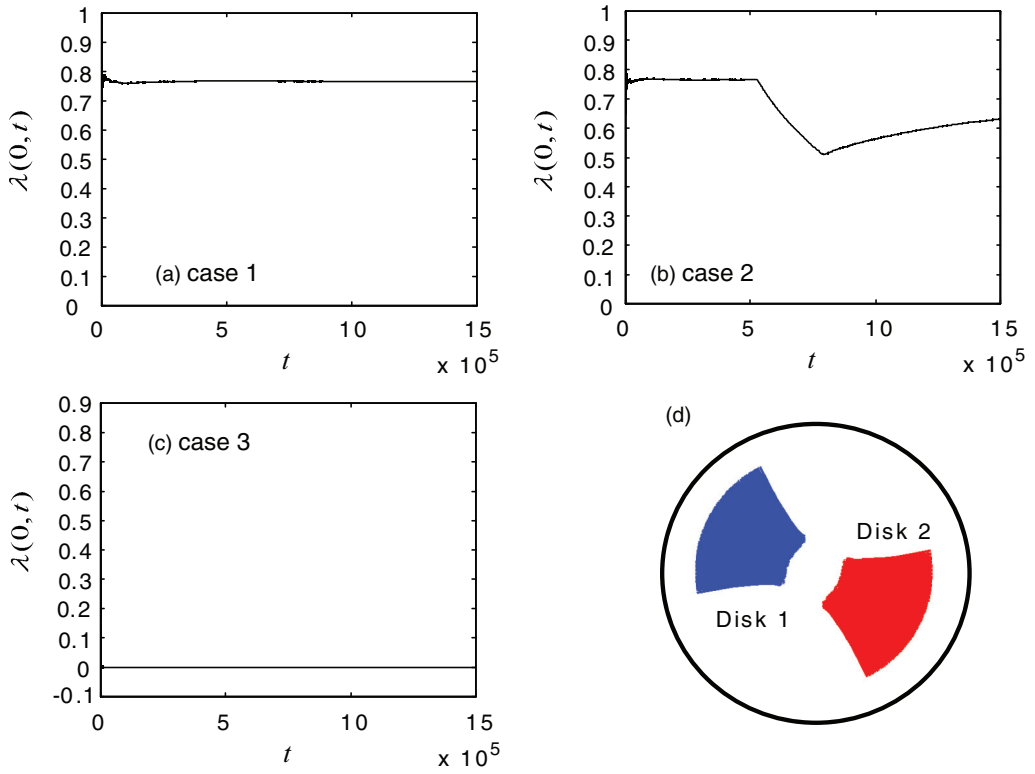

FIG. 3. (Color online) FTMLE as functions of the final time t, $\lambda(0,t)$, in the typical three cases for $\sigma = 2$: (a), (b), and (c) for the cases 1, 2, and 3, respectively. (d) The trajectories of centers of two disks in the case 3.

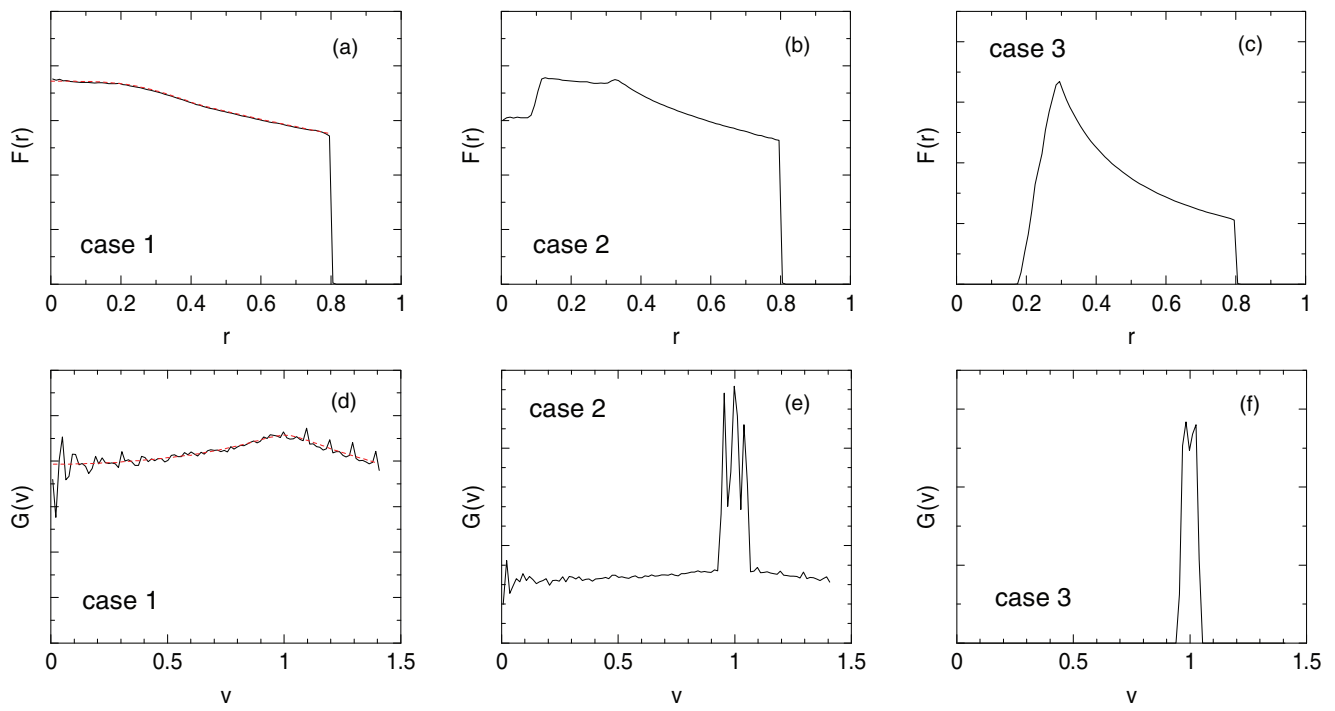

FIG. 4. (Color online) The configuration distributions in the upper panels and the velocity distributions in the lower panels in the three cases: (a) and (d) for the case 1, (b) and (e) for the case 2, (c) and (f) for the case 3, respectively. The solid and broken curves denote the distributions produced by the trajectories and the microcanonical distributions, respectively.

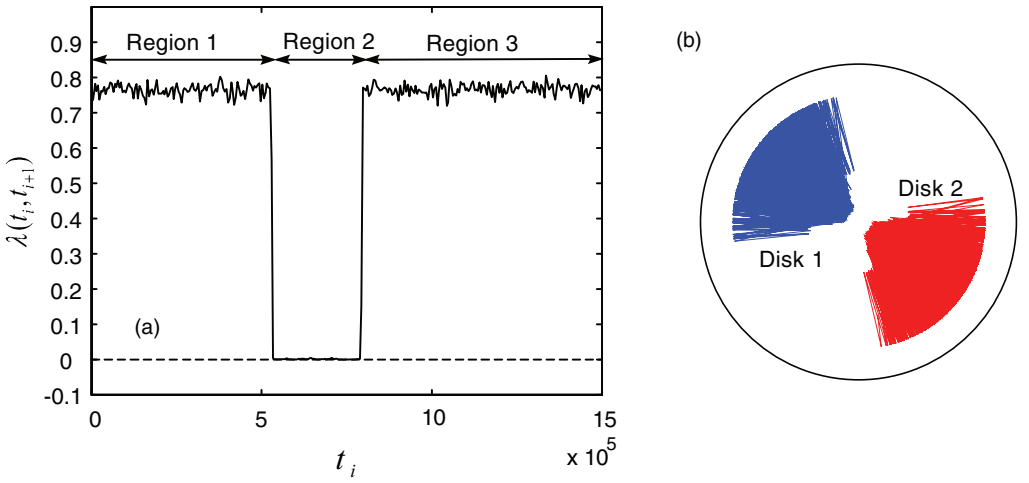

FIG. 5. (Color online) (a) FTMLE in each interval $\lambda(t_i,t_{i+1})$ for the case 2. (b) The trajectories in the region 2.

$r_1 = \sqrt{x_1^2 + y_1^2}$, we obtain

$$
\begin{aligned}
G(v_x,v_y) &\propto \int\cdots\int \delta(2-U^2-V^2-v^2)\delta(-r_1U + x_2v_y \\
&\quad - y_2v_x)dU\,dV\,dx_1dy_1dx_2dy_2 \\
&\propto \int\cdots\int \frac{1}{r_1}\delta\left[2-(x_2v_y-y_2v_x)^2/r_1^2 - V^2 - v^2\right] \\
&\quad \times dV\,dx_1dy_1dx_2dy_2 \\
&\propto \int\cdots\int \frac{1}{r_1}\delta(S^2-V^2)dV\,dx_1dy_1dx_2dy_2 \\
&\propto \iiiint_{D'} \frac{1}{r_1 S}dx_1dy_1dx_2dy_2, \qquad (15)
\end{aligned}
$$

where $v = \sqrt{v_x^2 + v_y^2}$ and $S = \sqrt{2-(x_2v_y - y_2v_x)^2/r_1^2 - v^2}$. The four-dimensional domain of integration D' is the accessible area of the first and second disks centered at $(x_1,\ y_1)$ and $(x_2,\ y_2)$, respectively, within the circular billiard. $G(v_x,v_y)$ should have circular symmetry, which is verified as follows. If we change x_i and y_i to $x_i' = (x_iv_x + y_iv_y)/v$, $y_i' = (y_iv_x - x_iv_y)/v$ $(i = 1,2)$, Eq. (14) is reduced to

$$
G(v_x,v_y) \propto \int\cdots\int_{D'} \frac{1}{\sqrt{(2-v^2)r_1^2 - y_2'^2v^2}}dx_1'dy_1'dx_2'dy_2'. \qquad (16)
$$

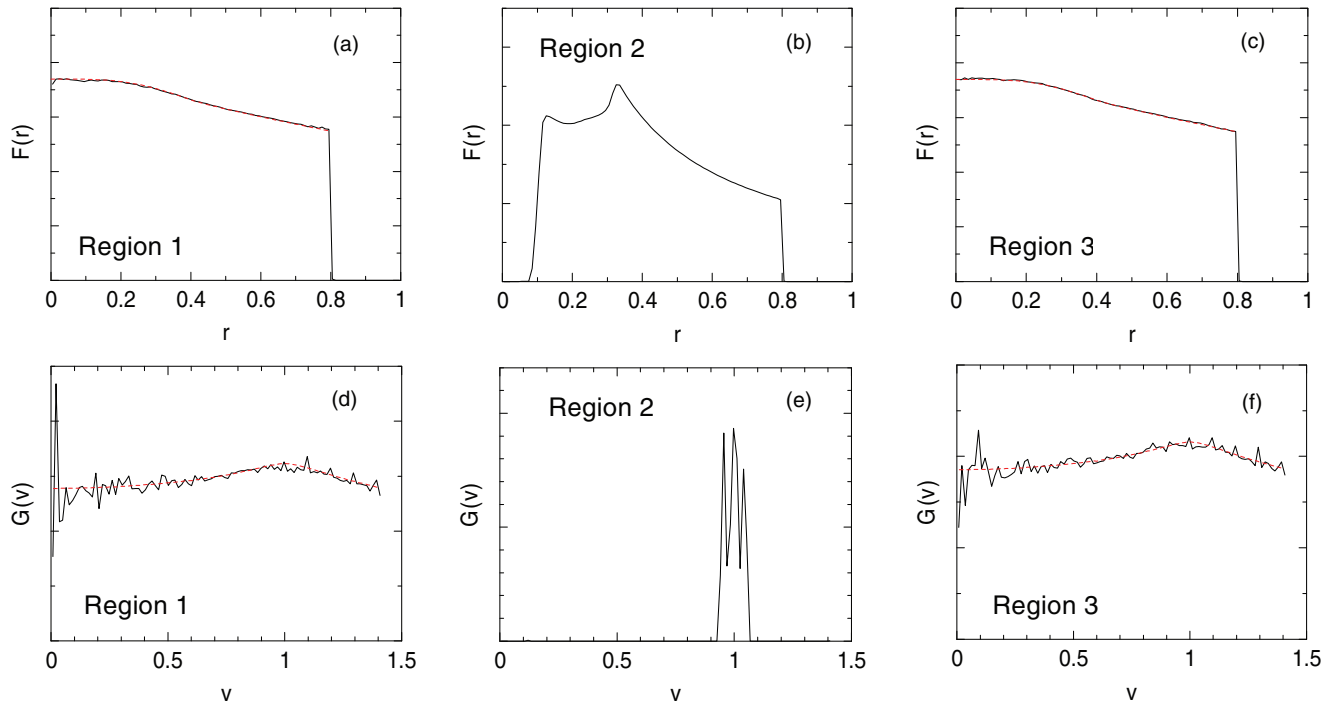

FIG. 6. (Color online) The configuration distributions in the upper panels and the velocity distributions in the lower panels for the case 2: (a) and (d) for the region 1, (b) and (e) for the region 2, (c) and (f) for the region 3, respectively.

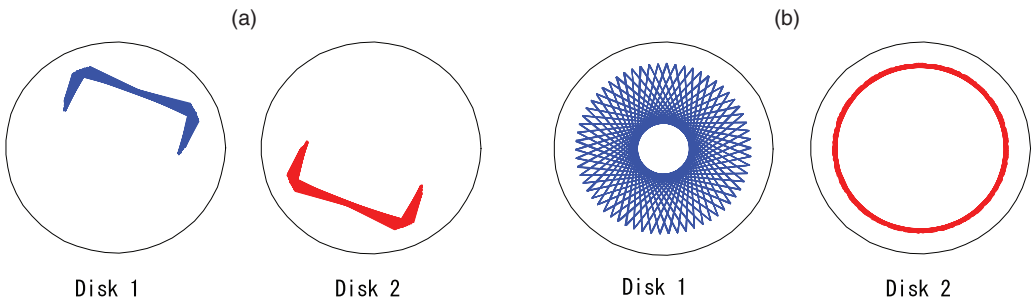

FIG. 7. (Color online) The trajectories of centers of two disks in two different types of quasiregular motions.

(Note that $r_1 = \sqrt{x_1^2 + y_1^2} = \sqrt{x_1'^2 + y_1'^2}$.) Hereafter, we use the expression $G(v)$ instead of $G(v_x, v_y)$. The detailed numerical technique of the integration is described in Appendix B.

In order to study a statistical character of the system, we prepare samples of initial conditions which are uniformly distributed in the phase space under the restriction of zero total angular momentum. For this purpose, we introduce the four-dimensional polar coordinates in the velocity space $(v,\theta,\varphi_1,\varphi_2)$ defined by [19]

$$\begin{cases} v_{x,1} = v\sin\theta\cos\varphi_1 \\ v_{y,1} = v\sin\theta\sin\varphi_1 \\ v_{x,2} = v\cos\theta\cos\varphi_2 \\ v_{y,2} = v\cos\theta\sin\varphi_2 \end{cases} \begin{pmatrix} 0 \leqslant v < \infty \\ 0 \leqslant \theta \leqslant \pi/2 \\ 0 \leqslant \varphi_1 \leqslant 2\pi \\ 0 \leqslant \varphi_2 \leqslant 2\pi \end{pmatrix}. \tag{17}$$

The infinitesimal volume element in the velocity space can be written as

$$dv_{x,1}dv_{y,1}dv_{x,2}dv_{y,2} = v^3\sin\theta\cos\theta\, dv\, d\theta\, d\varphi_1 d\varphi_2. \tag{18}$$

Then, the microcanonical ensemble distribution, Eq. (5), is rewritten as

$$\begin{aligned} &\rho(x_1,y_1,x_2,y_2,v,\theta,\varphi_1,\varphi_2)v^3\sin\theta\cos\theta\, dv\, d\theta\, d\varphi_1 d\varphi_2 dx_1 \\ &\quad\times dy_1 dx_2 dy_2 \\ &= C_N\delta(2-v^2)\delta(vK)2v^3\sin\theta\cos\theta\, dv\, d\theta\, d\varphi_1 d\varphi_2 \\ &\quad\times dx_1 dy_1 dx_2 dy_2, \end{aligned} \tag{19}$$

where

$$K = l_1\sin\theta + l_2\cos\theta \tag{20}$$

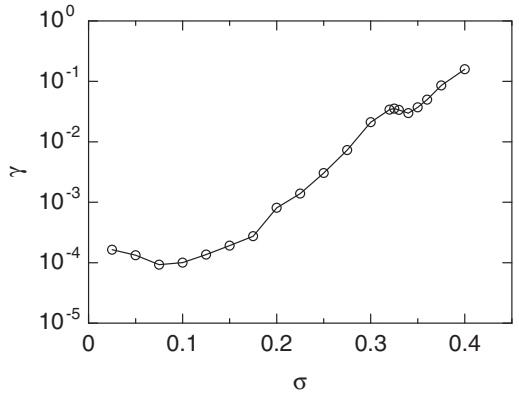

FIG. 8. Ratio of resident time in regular (or quasiregular) motions for various σ.

with $l_1 = x_1\sin\varphi_1 - y_1\cos\varphi_1$ and $l_2 = x_2\sin\varphi_2 - y_2\cos\varphi_2$. Integrating (19) with respect to v, we get the reduced distribution:

$$\begin{aligned} &P(x_1,y_1,x_2,y_2,\theta,\varphi_1,\varphi_2)\sin\theta\cos\theta\, d\theta\, d\varphi_1 d\varphi_2 dx_1 dy_1 dx_2 dy_2 \\ &\quad\propto \delta(K)\sin\theta\cos\theta\, d\theta\, d\varphi_1 d\varphi_2 dx_1 dy_1 dx_2 dy_2. \end{aligned} \tag{21}$$

If we introduce a variable $z = \sin^2\theta$, Eq. (21) is written as

$$\begin{aligned} &P(x_1,y_1,x_2,y_2,\varphi_1,\varphi_2,z)d\varphi_1 d\varphi_2 dz dx_1 dy_1 dx_2 dy_2 \\ &\quad\propto \delta(K)d\varphi_1 d\varphi_2 dz dx_1 dy_1 dx_2 dy_2, \end{aligned} \tag{22}$$

with

$$K = l_1\sqrt{z} + l_2\sqrt{1-z}. \tag{23}$$

Equation (22) suggests that we can use some generator of uniform random numbers for all variables to get initial conditions distributed uniformly in the phase space. The ranges of variables are as follows: $-1 \leqslant x_1,x_2,y_1,y_2 \leqslant 1, 0 \leqslant \varphi_1 \leqslant 2\pi$, $0 \leqslant \varphi_2 \leqslant 2\pi$, and $0 \leqslant z \leqslant 1$. After generating uniform random numbers and getting values of these variables, we pick up only sets of values satisfying the condition $x_1^2 + y_1^2 \leqslant (1-\sigma)^2$, $x_2^2 + y_2^2 \leqslant (1-\sigma)^2$, $(x_1 - x_2)^2 + (y_1 - y_2)^2 \geqslant 4\sigma^2$, and $K = 0$. The last condition, $K = 0$, is hard to get relevant values easily since they are quite rare. Therefore, we reduce it to a weaker condition $|K| < \varepsilon$ with some small value ε. After obtaining relevant values for all variables, we correct only the values of z to satisfy $K = 0$ exactly as follows. Solving the equation $K = 0$ with respect to z with the given values for other variables we have a unique solution for z,

$$z_0 = l_2^2/\left(l_1^2 + l_2^2\right), \tag{24}$$

which is used instead of the original value of z.

We also employ the four-dimensional polar coordinates for velocities of two disks to examine whether trajectories run over the phase space uniformly. In the six-dimensional space of coordinates $(x_1,x_2,y_1,y_2,\varphi_1,\varphi_2)$, we divide the region within $-1 \leqslant x_1,x_2,y_1,y_2 \leqslant 1, 0 \leqslant \varphi_1 \leqslant 2\pi$, $0 \leqslant \varphi_2 \leqslant 2\pi$ into a number of cells with an equal width in each dimension. When the values of x_1, x_2, y_1, y_2, φ_1, and φ_2 of a point on a trajectory are given, the value of z is automatically determined as (24). If a trajectory runs over the phase space uniformly, its density in each cell should be proportional to

$$\iiiiiint_{\text{cell}} \left[\int_0^1 \delta(K)dz\right] dx_1 dy_1 dx_2 dy_2 d\varphi_1 d\varphi_2. \tag{25}$$

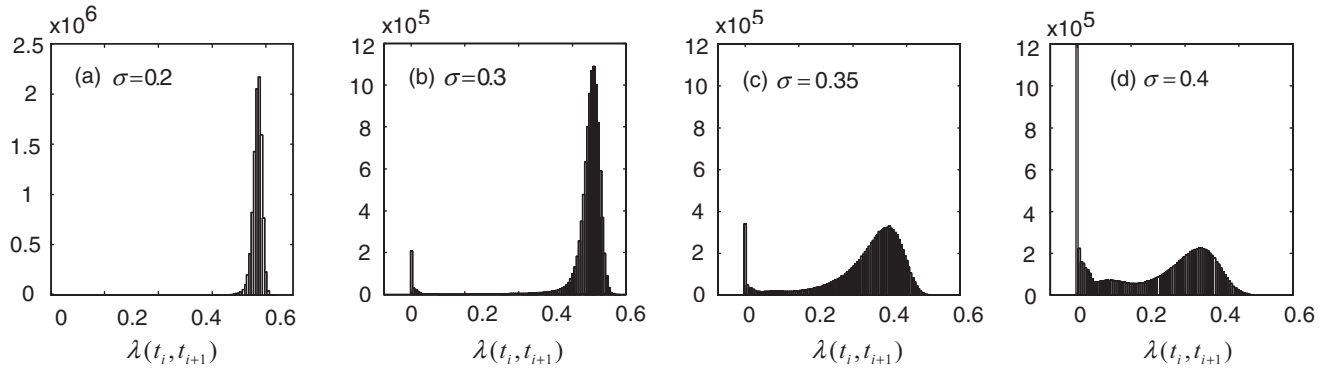

FIG. 9. The distributions of $\lambda(t_i,t_{i+1})$ for $\sigma = 0.2$, 0.3, 0.35, and 0.4, respectively.

The integration (25) is over only a region of the cell satisfying the conditions $x_1^2 + y_1^2 \leqslant (1-\sigma)^2$, $x_2^2 + y_2^2 \leqslant (1-\sigma)^2$, $(x_1 - x_2)^2 + (y_1 - y_2)^2 \geqslant 4\sigma^2$. Using the relation

$$\delta(K)dz = \left|\frac{\partial K}{\partial z}(z_0)\right|^{-1} \delta(z - z_0), \tag{26}$$

(25) is reduced to

$$\iint\iint\iint_{\text{cell}} \left|\frac{\partial K}{\partial z}(z_0)\right|^{-1} dx_1 dy_1 dx_2 dy_2 d\varphi_1 d\varphi_2. \tag{27}$$

It should be noted that the integration (27) is restricted to the region where the equation $K(z) = 0$ has a solution (24), i.e., $l_1 l_2 \leqslant 0$.

III. NUMERICAL RESULTS

In order to study a statistical character of the system, we first prepare samples of initial conditions which are uniformly distributed in the phase space under the restriction of zero total angular momentum. The sampling method has been described in the previous section. We chose 10^{-5} for ε in the constraint condition $|K| < \varepsilon$. We have prepared 10^5 initial conditions for each value of σ. The solid curves in Fig. 1 represent the single-particle configuration and velocity distributions produced by the sampling for several values of σ. The broken curves denote the microcanonical distributions. We see that the present sampling reproduces the microcanonical distributions very well. Note that the distributions produced by sampling do not necessarily have circular symmetry in general. We have averaged the original distributions over the angular direction to plot

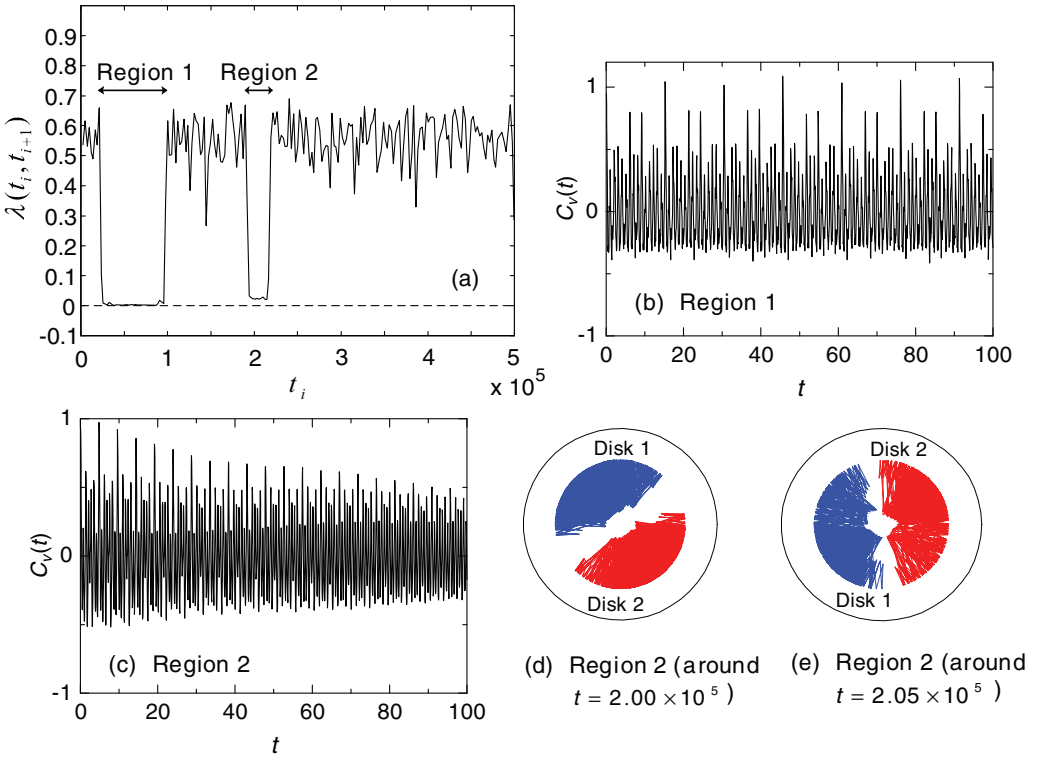

FIG. 10. (Color online) The results for $\sigma = 0.33$: (a) FTMLE in each interval $\lambda(t_i,t_{i+1})$, (b) and (c) the velocity autocorrelation functions for the regions 1 and 2, respectively, (d) and (e) the trajectories around $t = 2.00 \times 10^5$ and 2.05×10^5 in the region 2, respectively.

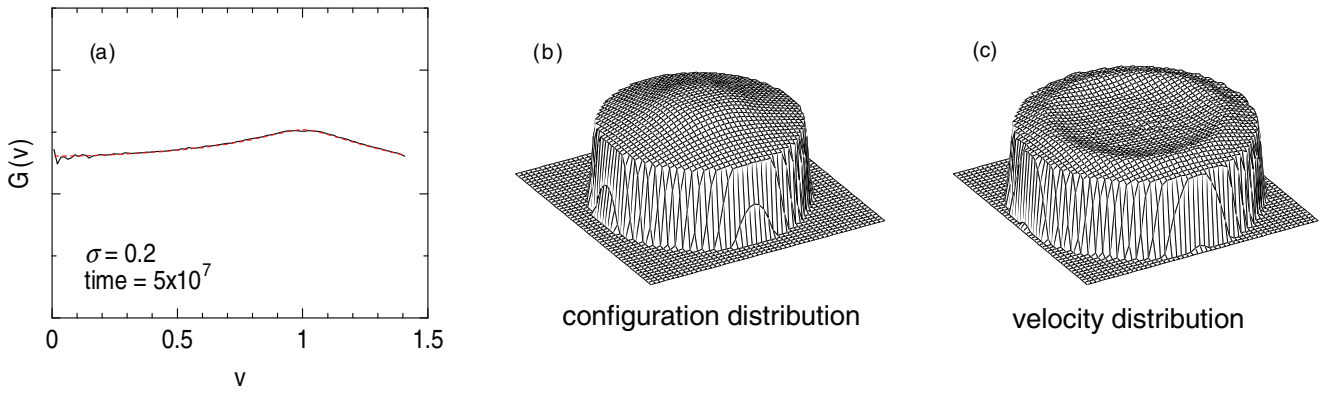

FIG. 11. (Color online) The distributions for $\sigma = 0.2$ from a trajectory with the running time of 5×10^7: (a) The velocity distribution. The angular dependence is shown in (b) and (c) for the configuration and velocity distributions, respectively.

the above distributions. We also take similar averages to plot distributions from dynamical trajectories calculations below.

We calculate FTMLE $\lambda(0,T)$ for each trajectory running over 10^6 collisions with the above initial condition, where T is the running time during 10^6 collisions. The values of $\lambda(0,T)$ for each σ depend on the initial conditions and distribute in some extent. The averaged values and standard deviation of $\lambda(0,T)$ for various σ are plotted in Figs. 2(a) and 2(b), respectively. It is seen that the averaged value of $\lambda(0,T)$ increases as σ increases from 0 to around 0.225 and then decreases with further increase of σ. The standard deviation is relatively small for $\sigma < 0.2$ and increases as σ increase except in $0.33 < \sigma < 0.35$.

Now we examine the detailed evolution of FTMLE. We show FTMLE as functions of the final time t, $\lambda(0,t)$, in the typical three cases for $\sigma = 0.2$ in Fig. 3. In the case 1, $\lambda(0,t)$ is almost constant and seems to converge. Its value is positive, which implies the motion is chaotic. In the case 2, its evolution makes an abrupt change twice. In the case 3, $\lambda(0,t)$ is almost constant and nearly equal to zero, which implies the trajectory stays in a torus. For the case 3, the trajectories of centers of two disks are illustrated in Fig. 3(d). The two disks vibrate regularly and symmetrically bouncing with each other. If we truncate the evolution of FTMLE at $t = T$, the three cases yield different values of $\lambda(0,T)$ in general. This is a main

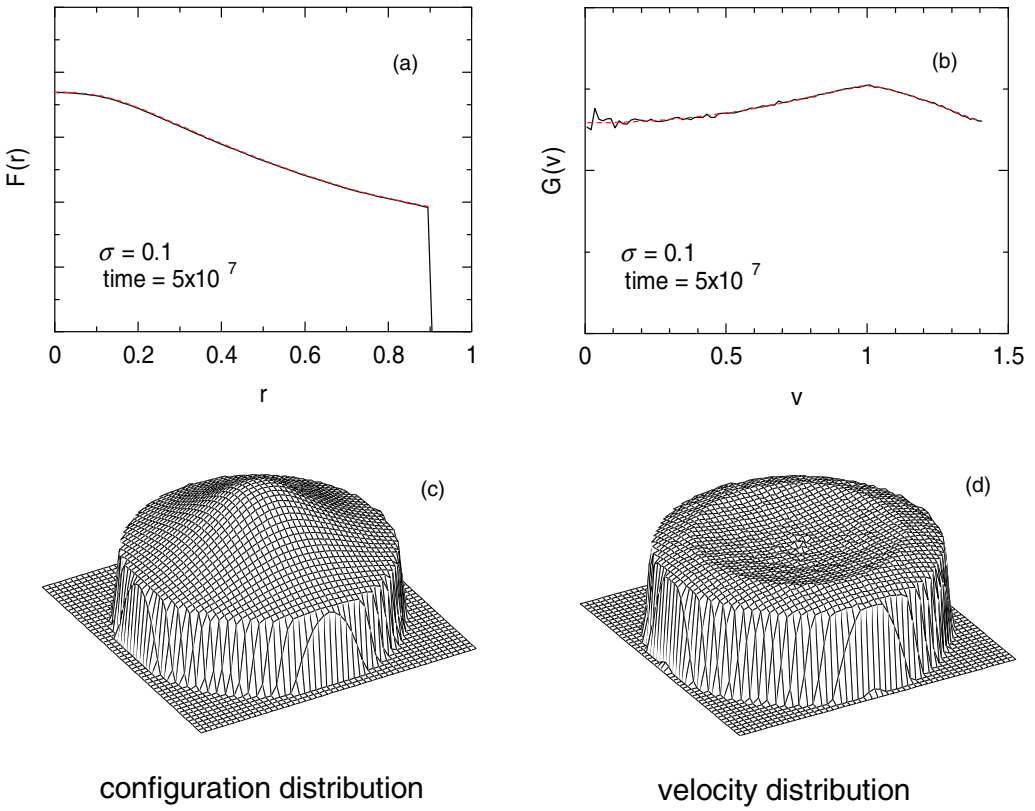

FIG. 12. (Color online) The distributions for $\sigma = 0.1$: (a) the configuration distribution and (b) the velocity distribution from a trajectory with running times of 5×10^7. The angular dependence is shown in (c) and (d) for the configuration and velocity distributions, respectively.

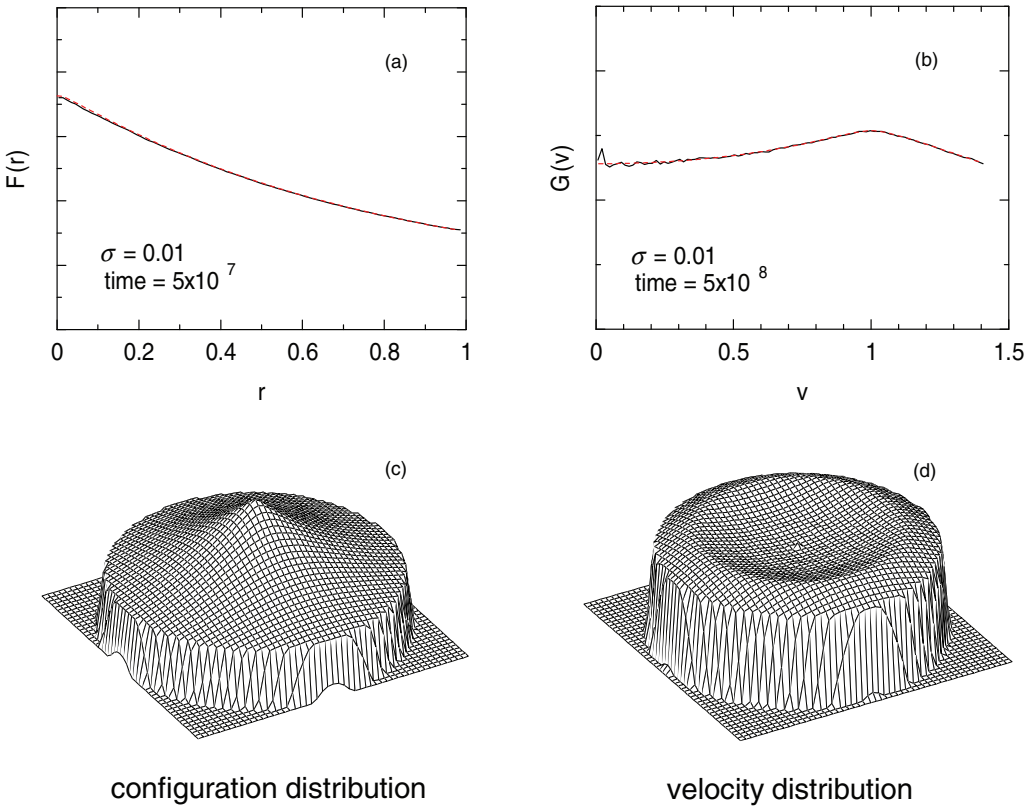

FIG. 13. (Color online) The same as Fig. 12 except for $\sigma = 0.01$ and different running times.

reason for the values of $\lambda(0,T)$ distributing in some extent for each σ. In Fig. 4, we show the single-particle configuration distributions in the upper panels and the velocity distributions in the lower panels produced by the trajectories in the three cases: Figs. 4(a) and 4(d) for the case 1, Figs. 4(b) and 4(e) for the case 2, Figs. 4(c) and 4(f) for the case 3, respectively. We see that the distributions produced by the trajectory in the case 1 (the solid curves) are in a good agreement with the microcanonical distributions (the broken curves).

Let us analyze the trajectory in the case 2 in detail. We divide the total period into multiple short-time intervals, each of which includes 10^4 collisions. We calculate FTMLE in each interval $\lambda(t_i,t_{i+1})$, where t_i is the initial time for the ith interval. Then, we obtain a sequence of $\lambda(t_i,t_{i+1})$, which is shown in Fig. 5(a). We see that the total period is composed of three time regions. In the regions 1 and 3, $\lambda(t_i,t_{i+1})$'s have positive values fluctuating around 0.77, which is almost equal to the constant value of $\lambda(0,t)$ in the case 1. On the other hand, they are almost equal to zero in the region 2. This fact implies that the system exhibits chaotic motions in the regions 1 and 3 while it exhibits a sticky motion, i.e., a quasiregular motion trapped around a torus in the region 2. The trajectories of centers of two disks in the region 2 are illustrated in Fig. 5(b). This sticky motion of two disks is quite similar to the one in the case 3. We calculate single-particle distributions produced by the trajectory in each region separately. The results are shown in Fig. 6, where the configuration distributions are in the upper panels and the velocity distributions in the lower panels : Figs. 6(a) and 6(d) for the region 1, Figs. 6(b) and 6(e) for the region 2, Figs. 6(c) and 6(f) for the region 3, respectively. We see that the distributions produced by the trajectories (the solid curves) in the regions 1 and 2 are in a good agreement with the microcanonical distributions (the broken curves). Let us call trajectories similar to those in the cases 1, 2, and 3 trajectories of the types 1, 2, and 3, respectively. For $\sigma = 0.2$, several percent of the 10^5 trajectories are of the type 2, in which we have found a lot of other kinds of quasiregular motions trapped around tori. However, most of them are similar to the one illustrated in Fig. 5(b). Only two of them are illustrated in Fig. 7 as essentially different types. In Fig. 7(b), two disks move independently without any pair collisions. Only about 0.1% of trajectories are of the type 3 for $\sigma = 0.2$. Trajectories of the type 2 are found even for $\sigma = 0.01$ and their number increases as σ increases. The number of the type 3 also increases as σ increases.

We calculate a ratio of resident time for trajectories in regular (or quasiregular) motions to a total running time for each value of σ. We assume that the motion in an interval $[t_i,\ t_{i+1}]$ is regular (or quasiregular) if the value of $\lambda(t_i,t_{i+1})$ is less than some small value, for which we choose 0.01. We accumulate time intervals corresponding to regular (or quasiregular) motions over all trajectories (10^5 trajectories) and get a total resident time in regular (or quasiregular) motions $T_{\rm r}$. On the other hand, we sum up running times over all trajectories and get a total running time $T_{\rm tot}$. Then, we obtain the ratio $\gamma = T_{\rm r}/T_{\rm tot}$. The results of γ for various values of σ are shown in Fig. 8. The values of γ for $\sigma < 0.2$ are of the order of 10^{-4}. It begins to increase exponentially around $\sigma = 0.2$, where the average of $\lambda(0,T)$ has a maximum value (see Fig. 2). From this fact, we can guess that tori in the phase space increase abruptly around $\sigma = 0.2$. It is seen that

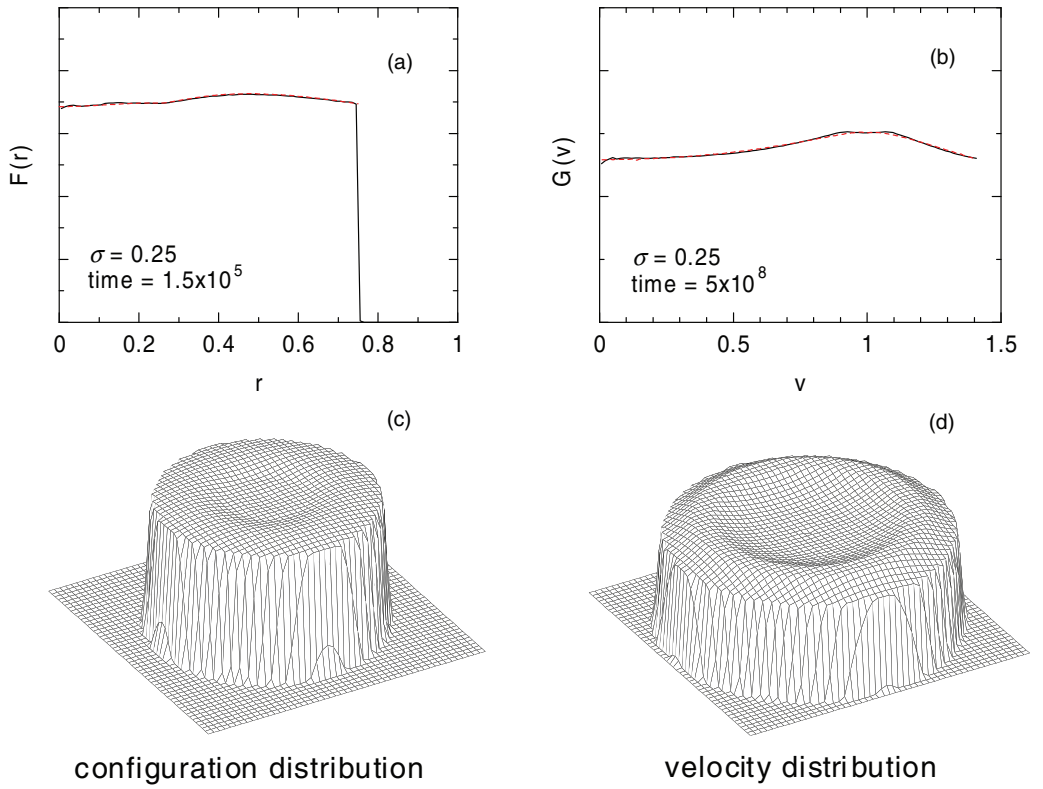

FIG. 14. (Color online) The same as Fig. 12 except for $\sigma = 0.25$ and different running times.

γ decreases as σ increases around $\sigma = 0.33$. This is not due to a statistical error. We have calculated γ for several different sets of initial conditions in this region of σ and obtained almost the same results. Figures 9(a)–9(d) show the distributions of $\lambda(t_i, t_{i+1})$ for $\sigma = 0.2, 0.3, 0.35$, and 0.4, respectively. It is seen that the deviation of the distribution increases as σ increases. It does not necessarily mean that there are various kinds of trajectories having different specific values of $\lambda(t_i, t_{i+1})$. It rather means that values of $\lambda(t_i, t_{i+1})$ along a single trajectory fluctuate more strongly as σ increases. Figure 10(a) shows the evolution of $\lambda(t_i, t_{i+1})$ along a typical trajectory for $\sigma = 0.33$. We see that there are two regions (the regions 1 and 2) in which the values of $\lambda(t_i, t_{i+1})$ are close to zero while they fluctuate strongly in other regions [cf. Fig. 5(a) for $\sigma = 0.2$]. In order to analyze motions in the regions 1 and 2, we calculate the velocity autocorrelation function given by

$$C_v(t) = \lim_{T\to\infty} \frac{1}{T} \int_0^T \boldsymbol{v}(\tau) \cdot \boldsymbol{v}(\tau + t) d\tau, \tag{28}$$

where $\boldsymbol{v}$ is a four-dimensional velocity vector for two disks, $\boldsymbol{v} = (v_{x,1}, v_{y,1}, v_{x,2}, v_{y,2})$. The results are shown in Figs. 10(b) and 10(c) for the regions 1 and 2, respectively. These figures show that the amplitude of $C_v(t)$ does not decrease in the region 1, where the values of $\lambda(t_i, t_{i+1})$ are almost equal to zero, so that the motion is almost regular. On the other hand, the amplitude of $C_v(t)$ decreases quite slowly in the region 2, where $\lambda(t_i, t_{i+1})$ has small positive values, so that the motion is quite weakly chaotic. The trajectories of centers of two disks in the region 1 are similar to Fig. 5(b). The motion in the region 2 is somewhat complicated. Figures 10(d) and 10(e) show the trajectories in two different short time regions around $t = 2.00 \times 10^5$ and 2.05×10^5, respectively, within the region 2, each of which includes about 1500 collisions. The disks vibrate quasiperiodically and the centers of the vibration move slowly. The traces of these motions are shaped in the form of a fan in both regions. The fan-shaped areas rotate gradually in a long time so that the amplitude of $C_v(t)$ decreases slowly.

In order to find any relation between the above fact and ergodicity of the system, we examine single-particle distributions from trajectories and compare them with the microcanonical distributions for various values of σ. Hereafter, we show not a statistical result but one for a single trajectory of the type 1, i.e., a nonsticky trajectory, in each case. We have already shown one of results for $\sigma = 0.2$ in Figs. 4(a) and 4(d), where we see that the single-particle distributions from the trajectory (the solid curves) are in a good agreement with the microcanonical distributions (the broken curves). Especially, the configuration distribution from the trajectory converges quite well to that in the microcanonical ensemble. We show a result of the velocity distribution for a longer trajectory with the same initial condition in Fig. 11(a). The running time of this trajectory is 5×10^7 while that of Fig. 4(d) is 1.5×10^5. We see that it also converges quite well to that in the microcanonical ensemble though its convergence is slower than that of the configuration distribution. Remember that we have averaged the original distributions from the trajectories over the angular direction to plot the above distributions. The angular dependence is shown in Figs. 11(b) and 11(c) for the configuration and velocity distributions, respectively. They are from the trajectory of the running time of 5×10^7. We see that they have almost completely circular symmetry.

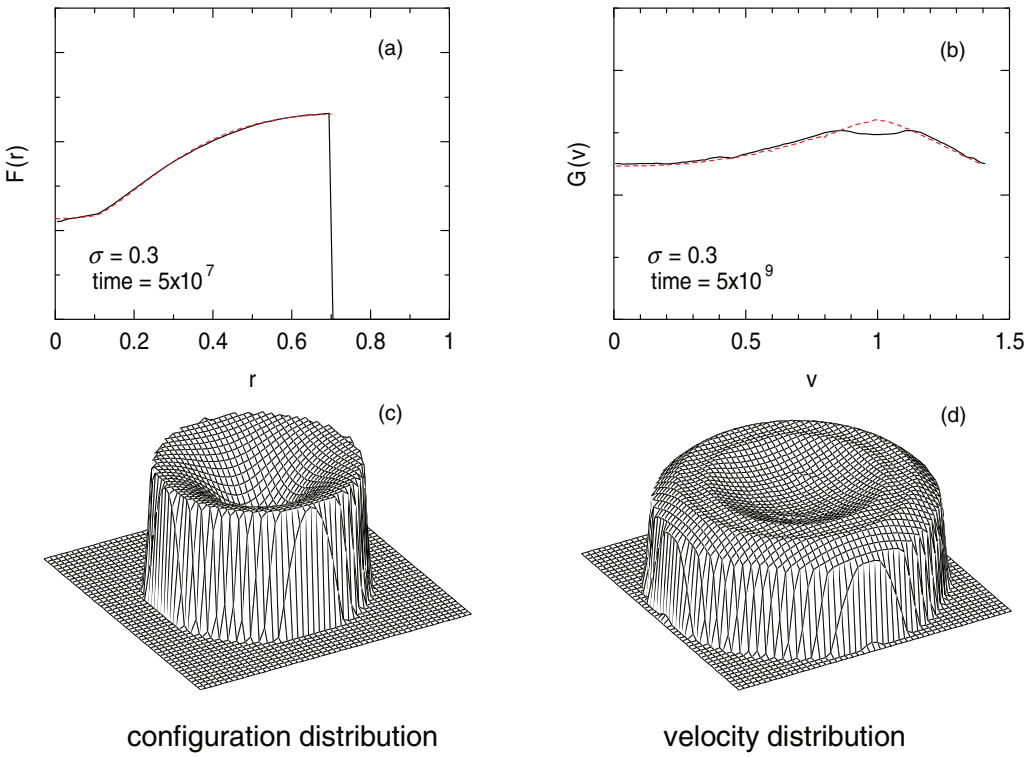

FIG. 15. (Color online) The same as Fig. 12 except for $\sigma = 0.3$ and different running times.

We have found similar results for $\sigma < 0.2$. For example, Figs. 12(a) and 12(b) show the results of the configuration and velocity distributions, respectively, for $\sigma = 0.1$. The solid curves denote the distributions from a trajectory with a running time of 5×10^7 while the broken curves denote the microcanonical distributions. Figures 12(c) and 12(d) show their angular dependence. We also show the results for a very small value of σ, $\sigma = 0.01$, in Fig. 13, where (a) and (b) show the results of the configuration and velocity distributions, respectively. The solid curves in Figs. 13(a) and 13(b) denote the configuration and velocity distributions from a trajectory, respectively. The running times are 5×10^7 and 5×10^8 in Figs. 13(a) and 13(b), respectively. Both of the distributions converge well to those in the microcanonical ensemble (the broken curve), although it takes more running time for the velocity distribution to converge. Figures 13(d) and 13(e) show their angular dependence. In this case, the number of pair collisions is about 2.4% of that of all collisions. In the time period of 5×10^8 pair collisions occur several 10^6 times, which yields a velocity distribution consistent with that in the microcanonical ensemble.

Now, we show results for $\sigma = 0.25$ in Fig. 14. The solid curve in Fig. 14(a) denotes the configuration distribution from a trajectory with a running time of 1.5×10^5. We see that it converges quite well to that in the microcanonical ensemble (the broken curve) similarly to the case of $\sigma = 0.2$. The solid curve in Fig. 14(b) denotes the velocity distribution from a trajectory with a running time of 5×10^8. While the velocity distribution from the trajectory is found to converge already at the running time 5×10^7, there is a slight discrepancy between those from a trajectory and in the microcanonical ensemble, i.e., the former has a small depression around $v = 1.0$. The angular dependence is shown in Figs. 14(c) and 14(d) for the configuration and velocity distributions, respectively. We see that they have almost completely circular symmetry similarly to the case $\sigma = 0.2$.

Next we show results for $\sigma = 0.3$ in Fig. 15. The solid curve in Fig. 15(a) denotes the configuration distribution from a trajectory with a running time of 5×10^7, which converges quite well to that in the microcanonical ensemble (the broken curve). The solid curves in Fig. 15(b) denotes the velocity distribution from a trajectory with a running time of 5×10^9, respectively, while the broken curve denotes that in the microcanonical ensemble. Although the velocity distribution converges at the running of 5×10^8, it has a larger depression around $v = 1.0$ than in the case of $\sigma = 0.25$. The angular dependence is shown in Figs. 15(c) and 15(d) for the configuration and velocity distributions. We see that the velocity distribution also has almost completely circular symmetry in spite of inconsistency with the microcanonical ensemble.

Finally, we show results for $\sigma = 0.33$, 0.35, and 0.4 in Fig. 16. The solid curves in Figs. 16(a), 16(b), and 16(c) denote velocity distributions from trajectories for $\sigma = 0.33$, 0.35, and 0.4, respectively, whose running times are 5×10^9. The broken curves denote those in the microcanonical ensemble. We see that the depression around $v = 1.0$, observed for $\sigma = 0.25$ and 0.3, grows up as σ increases. Moreover, a depression around $v = 0$ appears at $\sigma = 0.33$ and also grows up as σ increases. Figure 16(d) denotes the configuration distribution for $\sigma = 0.4$ from a trajectory with a running time of 5×10^7, which converges quite well to that in the microcanonical ensemble (the broken curve). The angular dependencies of the configuration and velocity distributions

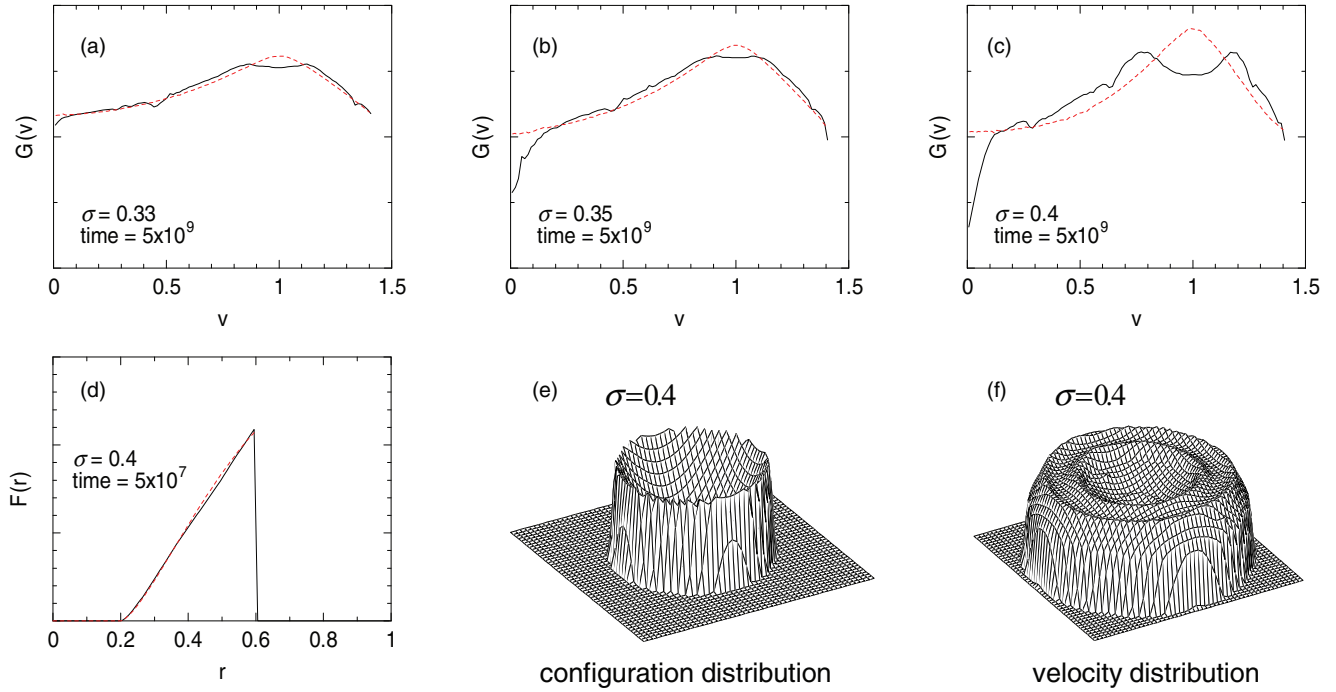

FIG. 16. (Color online) (a), (b), (c) Velocity distributions from trajectories with running time of 5×10^9 for $\sigma = 0.33$, 0.35, and 0.4, respectively. (d) The configuration distribution for $\sigma = 0.4$ from a trajectory with a running time of 5×10^7. (e), (f) The angular dependence of the configuration and velocity distributions, respectively, for $\sigma = 0.4$ from the trajectory of the running time of 5×10^9.

are shown for $\sigma = 0.4$ in Figs. 16(e) and 16(f), respectively, which are from the trajectory of the running time of 5×10^9. We see that they have almost circular symmetry even for $\sigma = 0.4$.

We further examine how trajectories spread over the energetically accessible region in the phase space. As described in the previous section, we employ the four-dimensional polar coordinates for velocities of two disks. The points on the trajectories are represented by the the six-dimensional coordinates $(x_1, y_1, x_2, y_2, \varphi_1, \varphi_2)$. We divide the region within $-1 \leqslant x_1, x_2, y_1, y_2 \leqslant 1$, $0 \leqslant \varphi_1 \leqslant 2\pi$, $0 \leqslant \varphi_2 \leqslant 2\pi$ into 20^6 cells (the region in each dimension is divided into 20 equal segments). Under the conditions of zero total angular momentum and nonoverlapping of two disks, each cell should be considered to have the volume given by (27), which is calculated numerically by the interpolatory quadrature method with the Chebyshev polynomials [20]. First we calculate time evolution of an occupied volume in the phase space. This is done by adding volumes of the cells one by one every time when the trajectory visits them for the first time. Actually, we pick up a point on a trajectory at every time interval $\Delta t = 0.01$ and examine which cell it is in. We do not count volumes of any cells twice. Figure 17(a) shows the results for time evolution of occupied volume normalized by the total volume of the energetically accessible region for $\sigma = 0.01$, 0.1, 0.2, 0.3, and 0.4, respectively. These results are for nonsticky trajectories whose configuration and velocity distributions are shown in Figs. 11–16. We see that their values do not increase smoothly but stay for a while and then suddenly increase. Therefore, one might imagine that the trajectories sometimes stay within

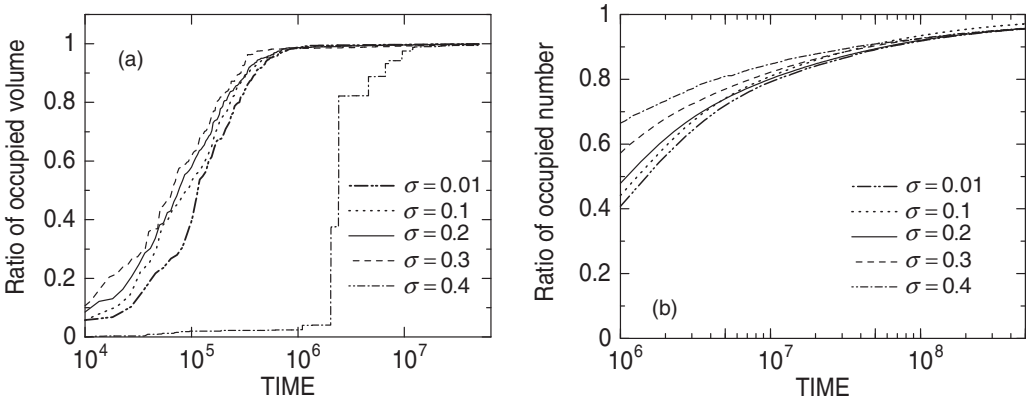

FIG. 17. The time evolution of occupied volume and a number of occupied cells in (a) and (b), respectively.

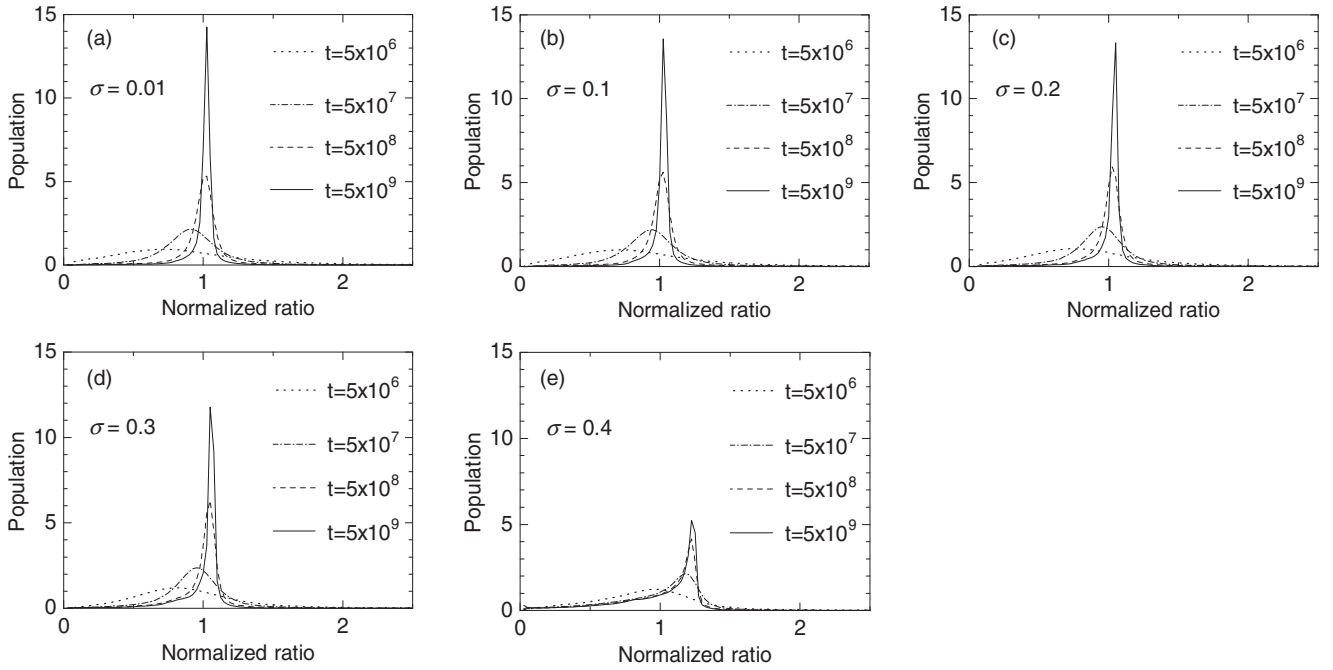

FIG. 18. The time evolution of the population for various values of σ.

some areas for a long time. However, it is not the case. The volumes of cells have a very wide distribution. Although the trajectories almost keep on going into another new cell, they enter sometimes into cells having smaller volumes and in other time into those having larger volumes. This causes unsmooth increase of the occupied volume. It is verified as follows. We calculate time evolution of a number of occupied cells instead of their volumes. Figure 17(b) shows the results for $\sigma = 0.01$, 0.1, 0.2, 0.3, and 0.4, respectively. We see that a number of occupied cells increase rather smoothly. It saturates very slowly since there are a lot of cells having small volumes and it takes a long time for the trajectories to pass all of them. From these figures, we can expect that a number of occupied cells tend to a total number of cells in the energetically accessible region in the limit of infinite time even for $\sigma = 0.4$. This suggests that tori are thinner than the present cells and possibly extend over a number of cells.

We also examine whether the trajectories run over the phase space uniformly. This time we accumulate a number of points on the trajectory in each cell every time when the trajectory visits it. Then, we divide each accumulated number by the volume of each cell given by (27). If a population of these ratios has a sharp peak around its mean value, we can conclude that the trajectory spreads over the phase space uniformly. The time evolution of the population is shown in Fig. 18, where the horizontal axis denotes the above ratio normalized by its mean value. These figures show that the trajectories for $\sigma =$ 0.01, 0.1, 0.2, and 0.3 gradually spread over almost uniformly while that for $\sigma = 0.4$ spreads nonuniformly. This is consistent with the results for the configuration and velocity distributions obtained from trajectories, although the discrepancy in the velocity distribution for $\sigma = 0.3$ seen in Fig. 15 is not well reflected in this result.

IV. SUMMARY AND CONCLUSION

We have investigated dynamical properties of the system of two identical hard disks within a circular billiard having a radius of unity. We confined our studies to the case of zero total angular momentum. Varying the radius of each disk σ, we have examined the chaotic dynamics and ergodicity of the system. We have found that the present system has a lot of KAM tori situated in a chaotic sea even for small values of σ. This causes chaotic and quasiregular motions possibly to coexist even in individual trajectories and the convergence of the maximum Lyapunov exponent to be quite slow. We used the finite-time maximum Lyapunov exponent (FTMLE) instead of the infinite-time one to characterize the dynamics of the system. Numerical results showed that there are three types of trajectories. In the case of the type 1, FTMLE is almost constant and seems to converge. Its value is positive, which implies the motion is chaotic. In the case of the type 2, there are two kinds of regions. FTMLE has positive values fluctuating around some value in the region of the chaotic irregular motion, while it has values almost equal to zero in the region of the quasiregular motion where the trajectory is trapped around a torus. In the case of the type 3, FTMLE is almost constant and nearly equal to zero, which implies the trajectory stays in a torus.

For each value of σ we calculated a sum of resident times in regular or quasiregular motions for 10^5 different trajectories and divided it by a sum of total running times for all trajectories. This ratio is of the order of 10^{-4} for $\sigma < 0.2$. It begins to increase exponentially around $\sigma = 0.2$, which suggests that tori in the phase space increase abruptly around $\sigma = 0.2$.

We also examined single-particle distributions from trajectories and compared them with those in the microcanonical ensemble for various values of σ. We calculated them for a

single trajectory of the type 1 in each case, which is considered to run without being trapped around any tori. We found that the configuration distributions obtained from trajectories are in a good agreement with those in the microcanonical ensemble for $\sigma = 0.01$ through 0.4. On the other hand, the velocity distributions obtained from trajectories are in a good agreement with those in the microcanonical ensemble for $\sigma \leqslant 0.2$, while some discrepancies between them are found for $\sigma \gtrsim 0.25$.

Consequently, we conclude that a number of tori in the phase space increase abruptly as σ increases beyond around 0.2 and tori prevent trajectories to move over the phase space uniformly, which makes the ergodicity of the system broken down. On the other hand, the present system is almost ergodic for $\sigma \leqslant 0.2$. This was also confirmed by showing that nonsticky trajectories run over the phase space uniformly for $\sigma \leqslant 0.2$.

We can extend this study on a circular billiard to the cases of nonzero total angular momentum and/or more than two hard disks. Uranagase found in the case of nonzero total angular momentum a smaller statistical fluctuation of the pressure evaluated by trajectory calculations even for a large value of σ than in the cases of zero total angular momentum (see Fig. 2 in Ref. [17]), which may imply ergodicity in such cases. Lansel *et al*. suggested nonergodicity in the cases of three and four disks [11]. Detailed studies in those cases are left for future works.

Finally, we refer to one more extension of this study. Recently, various billiards with time-dependent boundaries have been studied. If the billiard boundary is perturbed in time, depending on the geometry of the billiard boundary and on the initial conditions, the particle can accumulate energy along its trajectory, leading to a phenomenon called Fermi acceleration [21]. The following conjecture, known as Loskutov-Ryabov-Akinshin conjecture, has been proposed [22]: The Fermi acceleration will be observed in time-dependent billiards if the corresponding fixed-boundary billiards exhibit chaotic properties. This conjecture has been confirmed for various billiards [23–26]. However, those works are limited to single-particle systems and an extension to many-particle systems should be an interesting study.

APPENDIX A

In this Appendix, we describe the numerical technique for calculating the integral

$$I(r) = \int\int_D \frac{1}{\sqrt{r^2 + r_2^2}} dx_2 dy_2, \tag{A1}$$

where $r_2 = \sqrt{x_2^2 + y_2^2}$. The domain of integration D is the accessible area of the second disk centered at $(x_2,\ y_2)$ when the first disk is centered at $(x,\ y)$ within the circular billiard $(r = \sqrt{x^2 + y^2})$. This two-dimensional integral is reduced to a one-dimensional integral as follows. We rewrite $I(r)$ as a difference of two terms:

$$I(r) = I_0(r) - I_1(r). \tag{A2}$$

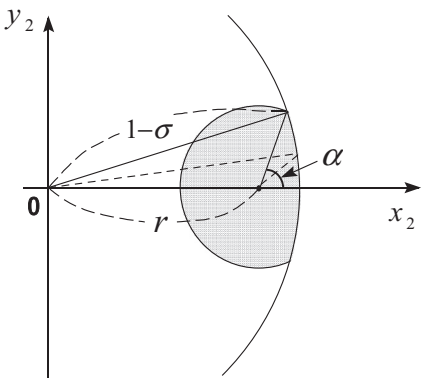

FIG. 19. The domain of integration.

$I_0(r)$ is the integral without respect to the overlap of two disks and given by

$$\begin{aligned} I_0(r) &= \iint_{x_2^2+y_2^2 \leqslant (1-\sigma)^2} \frac{1}{\sqrt{r^2 + r_2^2}} dx_2 dy_2 \\ &= 2\pi(\sqrt{(1-\sigma)^2 + r^2} - r). \end{aligned} \tag{A3}$$

$I_1(r)$ is the integral over the area of $(x_2,\ y_2)$ $\overline{D}$ in which the second disk centered at $(x_2,\ y_2)$ overlaps with the first disk centered at $(x,\ y)$:

$$I_1(r) = \iint_{\overline{D}} \frac{1}{\sqrt{r^2 + r_2^2}} dx_2 dy_2. \tag{A4}$$

We assume the first disk to be centered at $(0,r)$ without loss of generality. For $0 \leqslant r < 1 - 3\sigma$, the domain $\overline{D}$ is an inside of a circle having a radius of 2σ and centered at $(0,r)$. Changing the variables x_2 and y_2 to ρ and ϕ defined by $x_2 = r + \rho\cos\phi$ and $y_2 = \rho\sin\phi$, we obtain the expression

$$I_1(r) = 2\int_0^{\pi} g(2\sigma,\phi;r) d\phi, \tag{A5}$$

where the function $g(s,\phi;r)$ is given by

$$\begin{aligned} g(s,\phi;r) &= \int_0^s d\rho \frac{\rho}{\sqrt{\rho^2 + 2r\cos\phi\rho + 2r^2}} \\ &= \sqrt{s^2 + 2r\cos\phi s + 2r^2} - \sqrt{2}r - r\cos\phi \ln \\ &\quad \times \left| \frac{s + r\cos\phi + \sqrt{s^2 + 2r\cos\phi s + 2r^2}}{r\cos\phi + \sqrt{2}r} \right|. \end{aligned} \tag{A6}$$

For $1 - 3\sigma < r < 1 - \sigma$, $\overline{D}$ is the shadowed part illustrated in Fig. 19. The integral $I_1(r)$ can be written as

$$I_1(r) = 2\left(\int_0^{\alpha} g[R(\phi),\phi;r] d\phi + \int_{\alpha}^{\pi} g(2\sigma,\phi;r) d\phi \right) \tag{A7}$$

with

$$R(\phi) = -r\cos\phi + \sqrt{r^2(\cos^2\phi - 1) + (1-\sigma)^2} \tag{A8}$$

and

$$\alpha = \cos^{-1}\left(\frac{(1-\sigma)^2 - r^2 - 4\sigma^2}{4\sigma r} \right). \tag{A9}$$

APPENDIX B

In this Appendix, we describe the numerical technique for calculating the integral

$$J(v)=\iiiint_{D'}\frac{1}{\sqrt{(2-v^2)r_1^2-y_2^2v^2}}dx_1dy_1dx_2dy_2, \tag{B1}$$

where $r_1=\sqrt{x_1^2+y_1^2}$. The domain of integration D' is the accessible area of the first and second disks centered at $(x_1,\ y_1)$ and $(x_2,\ y_2)$, respectively, within the circular billiard. This four-dimensional integral is reduced to a one-dimensional integral plus a two-dimensional integral as shown below.

We rewrite $J(r)$ as a difference of two terms:

$$J(v)=J_0(v)-J_1(v). \tag{B2}$$

$J_0(v)$ is the integral without respect to the overlap of two disks and given by

$$J_0(v)=\iint_{x_1^2+y_1^2\leqslant(1-\sigma)^2}dx_1dy_1\iint_{x_2^2+y_2^2\leqslant(1-\sigma)^2}\times dx_2dy_2\,\frac{1}{\sqrt{(2-v^2)r_1^2-y_2^2v^2}}. \tag{B3}$$

$J_1(v)$ is the integral over the four-dimensional area $\overline{D'}$ in which the first and second disks overlap with each other:

$$J_1(v)=\iiiint_{\overline{D'}}\frac{1}{\sqrt{(2-v^2)r_1^2-y_2^2v^2}}dx_1dy_1dx_2dy_2. \tag{B4}$$

The integral $J_0(v)$ is reduced to a one-dimensional integral as follows:

$$\begin{aligned}J_0(v)&=\int dy_2\int_{-\sqrt{r_c^2-y_2^2}}^{\sqrt{r_c^2-y_2^2}}dx_2\iint_{x_1^2+y_1^2\leqslant r_c^2}\times dx_1dy_1\frac{1}{\sqrt{(2-v^2)r_1^2-y_2^2v^2}}\\&=\frac{4}{v_c}\int_0^{r_c}dz\sqrt{r_c^2-z^2}\left(\iint_{x_1^2+y_1^2\leqslant r_c^2}\frac{dx_1dy_1}{\sqrt{r_1^2-z^2v^2/v_c^2}}\right),\end{aligned} \tag{B5}$$

where $r_c=1-\sigma$ and $v_c=\sqrt{2-v^2}$. Introducing the polar coordinates r_1 and θ_1 ($x_1=r_1\cos\theta_1$ and $y_1=r_1\sin\theta_1$), we obtain an analytical expression for the integral in the parentheses of Eq. (B5). Then, we have

$$J_0(v)=\frac{8\pi}{v_c}\int_0^{r_c}\sqrt{r_c^2-z^2}\sqrt{r_c^2-z^2v^2/v_c^2}\,dz. \tag{B6}$$

Next, we consider $J_1(v)$. Introducing the polar coordinates r_1 and θ_1 ($x_1=r_1\cos\theta_1$ and $y_1=r_1\sin\theta_1$) again, we have

$$J_1(v)=\frac{2\pi}{v_c}\int_0^{1-\sigma}h(r)dr, \tag{B7}$$

with

$$h(r)=\iint_{\overline{D}}\frac{r}{\sqrt{r^2-y_2^2v^2/v_c^2}}dx_2dy_2. \tag{B8}$$

The domain of integration $\overline{D}$ is the area of $(x_2,\ y_2)$ in which the second disk centered at $(x_2,\ y_2)$ overlaps with the first disk centered at $(0,r)$. Equation (B8) is reduced to the one-dimensional integral as shown below, so that $J_1(v)$ is reduced to the two-dimensional integral. We need somewhat tedious geometric consideration to derive those expressions. We just show the results without derivation. In the case of $\sigma<1/3$, Eq. (B8) is reduced to

$$h(r)=2\int_0^{\pi}\rho_c(r,\phi)\big(\rho_c(r,\phi)-\sqrt{\rho_c^2-\mathrm{Min}(2\sigma,\rho_c)^2}\big)d\phi \tag{B9}$$

for $r<1-3\sigma$, and

$$\begin{aligned}h(r)=2\Bigg(&\int_0^{\alpha}\rho_c(r,\phi)\big(\rho_c(r,\phi)-\sqrt{\rho_c^2-\mathrm{Min}[R(\phi),\rho_c]^2}\big)d\phi\\&+\int_{\alpha}^{\pi}\rho_c(r,\phi)\big(\rho_c(r,\phi)-\sqrt{\rho_c^2-\mathrm{Min}(2\sigma,\rho_c)^2}\big)d\phi\Bigg)\end{aligned} \tag{B10}$$

for $r>1-3\sigma$, where

$$\rho_c(r,\phi)=\frac{rv_c}{v\sin\phi}, \tag{B11}$$

$$\alpha=\cos^{-1}\left(\frac{(1-\sigma)^2-r^2-4\sigma^2}{4\sigma r}\right), \tag{B12}$$

and

$$R(\phi)=-r\cos\phi+\sqrt{r^2(\cos^2\phi-1)+(1-\sigma)^2}. \tag{B13}$$

In the case of $\sigma>1/3$, Eq. (B8) is reduced to

$$h(r)=2\int_0^{\pi}\rho_c(r,\phi)\big(\rho_c(r,\phi)-\sqrt{\rho_c^2-\mathrm{Min}(1-\sigma,\rho_c)^2}\big)d\phi \tag{B14}$$

for $r<3\sigma-1$ and Eq. (B10) for $r>3\sigma-1$.

[1] R. Jancel, *Foundations of Classical and Quantum Statistical Mechanics* (Pergamon, Oxford, 1969).

[2] N. S. Krylov, *Works on the Foundations of Statistical Physics* (Princeton University Press, Princeton, NJ, 1979).

[3] *Dynamical Systems: Collection of Papers*, edited by Ya G. Sinai (World Scientific, Singapore, 1991).

[4] *Dynamical Systems, Ergodic Theory and Applications*, edited by Ya G. Sinai (Springer, Berlin, 2000).

[5] L. E. Reichl, *The Transition to Chaos* (Springer, Berlin, 1992).

[6] V. Berdichevsky, *Thermodynamics of Chaos and Order* (Addison Wesley Longman, London, 1997).
[7] *Hard Ball Systems and the Lorentz Gas*, edited by D. Szász (Springer, Berlin, 2000).
[8] N. Chernov and R. Markarian, *Chaotic Billiards* (American Mathematical Society, Providence, RI, 2006).
[9] K. Nakamura and T. Harayama, *Quantum Chaos and Quantum Dots* (Oxford University Press, Oxford, 2004).
[10] L. A. Bunimovich, Chaos **13**, 903 (2003).
[11] S. Lansel, M. A. Porter, and L. A. Bunimovich, Chaos **16**, 013129 (2006).
[12] S. Ranković and M. A. Porter, Chaos **23**, 013123 (2013).
[13] T. Munakata and M. Uranagase, in *Progress in Statistical Mechanics Research*, edited by J. S. Moreno (Nova Science, New York, 2008), Chap. 4, and references there.
[14] Z. Zheng, G. Hu, and J. Zhang, Phys. Rev. E **53**, 3246 (1996).
[15] N. Simányi, Ergodic Theory Dynam. Syst. **19**, 741 (1999).
[16] P. Bálint and S. Troubetzkoy, Nonlinearity **17**, 2069 (2004).
[17] M. Uranagase, Phys. Rev. E **76**, 061111 (2007).
[18] N. Nakazono, T. Kato, and K. Nakamura, Chaos, Solitons, and Fractals **23**, 1351 (2005).
[19] http://www5.ocn.ne.jp/coast/math-science/math/polar-coordinates.html (in Japanese).
[20] T. Tsuda, Numerishe Mathematik **20**, 377 (1973).
[21] E. Fermi, Phys. Rev. **75**, 1169 (1949).
[22] A. Loskutov, A. B. Ryabov, and L. G. Akinshin, J. Phys. A: Math. Gen. **33**, 7973 (2000).
[23] A. Loskutov and A. B. Ryabov, J. Stat. Phys. **108**, 995 (2002).
[24] R. E. de Carvalho, F. C. de Sousa, and E. D. Leonel, J. Phys. A: Math. Gen. **39**, 3561 (2006).
[25] E. D. Leonel, D. F. M. Oliveira, and A. Loskutov, Chaos **19**, 033142 (2009).
[26] V. Gelfreich and D. Turaev, J. Phys. A: Math. Theor. **41**, 212003 (2008).